Nano Research

Open Access

Research Article

# Enhanced high-energy-density $WO_3$-based electrochromic batteries via acid-modified graphite foil cathode

Yingyu Chen[1,§], Jiangbei Wan[1,§], Chenyang Zhang[1], Xueqing Tang[2]✉, Lu Chen[1], Zengxian Tang[1], De Li[1], Yong Chen[3]✉, Changhong Wang[4], Shan Cong[2], Zhigang Zhao[2], and Zhen Wang[1]✉

[1] *Key Laboratory of Research on Utilization of Si-Zr-Ti Resources of Hainan Province, School of Materials Science and Engineering, Hainan University, Haikou 570228, China*
[2] *Key Lab of Nanodevices and Applications, Suzhou Institute of Nano-Tech and Nano-Bionics Chinese Academy of Sciences (CAS), Suzhou 215123, China*
[3] *Guangdong Key Laboratory for Hydrogen Energy Technologies, School of Materials Science and Hydrogen Energy, Foshan University, Foshan 528000, China*
[4] *School of Materials Science and Engineering, Suzhou University of Science and Technology, Suzhou 215009, China*
§ *Yingyu Chen and Jiangbei Wan contributed equally to this work.*

**Cite this article:** *Nano Research*, **2025**, *18*, 94907799. https://doi.org/10.26599/NR.2025.94907799

**ABSTRACT:** In conventional tungsten oxide-based electrochromic batteries (ECBs), tungsten oxide acts as the cathode and Zn foil as the anode, but low redox potential leads to a limited discharge plateau, low areal capacitance, and power density, restricting practical applications. In this study, a novel $WO_3$||acid-modified graphite foil ($WO_3$||AGF) ECB was developed using AGF as the cathode, $WO_3$ as the anode, and a hybrid $Zn^{2+}/Al^{3+}$ electrolyte. The AGF offers advantages, such as high ion storage capacity, fast kinetics, and a high electrode potential, ensuring a high discharge voltage and capacity for the $WO_3$||AGF ECB. The prepared $WO_3$||AGF ECB not only exhibits excellent electrochromic performance but also demonstrates superior energy storage capabilities. At a charge/discharge current density of 0.5 mA·cm$^{-2}$, the $WO_3$||AGF ECB achieves a stable discharge capacity of 315.6 mAh·m$^{-2}$, which is 7.8 times higher than that of the traditional Zn||$WO_3$ ECB. Moreover, the rapid ion diffusion kinetics of the AGF ensure the cycling stability of the device at high voltages, maintaining 94.4% optical modulation after 8000 coloring/bleaching cycles. This work provides a novel approach by designing more compatible electrode material systems to achieve ECBs with high energy and power densities.

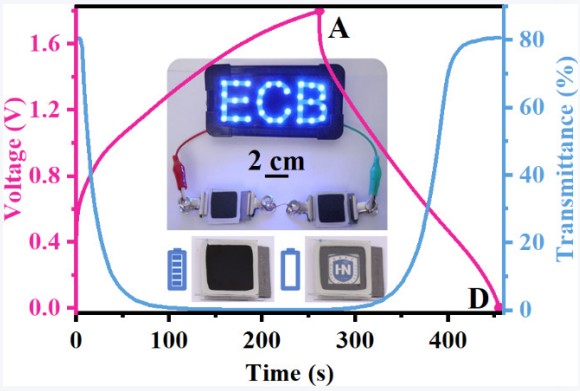


**KEYWORDS:** electrochromic batteries, high energy density, graphite foil, $WO_3$

## 1 Introduction

With the increasing interest in energy-efficient smart windows and displays, the integration of electrochromism and energy storage functionalities into a single device emerges as a promising strategy [1, 2]. It is noteworthy that electrochromic devices (ECDs) share structural and mechanistic similarities with ion batteries. Hence, integrating them into an electrochromic battery (ECB) is feasible [3, 4]. This integration offers two potential applications for achieving a sustainable energy society: Firstly, establishing intelligent battery systems capable of real-time and intuitive display of energy storage levels; secondly, developing the next generation of electrochromic devices that can recycle and utilize consumed energy, thereby significantly reducing the energy consumption of electrochromic devices [5, 6]. Tungsten oxide, owing to its high optical modulation and exceptional structural stability, stands out as the most widely applied and extensively researched electrochromic material [7–9], gaining favor among researchers in the field of ECBs. For instance, Al||$W_{18}O_{49}$ ECBs are constructed by utilizing $W_{18}O_{49}$ film as the cathode, Al foil as the anode, and $AlCl_3$ solution

**Received:** March 27, 2025; **Revised:** May 23, 2025
**Accepted:** July 14, 2025

✉Address correspondence to Zhen Wang, zwang2020@hainanu.edu.cn; Xueqing Tang, xqtang2019@sinano.ac.cn; Yong Chen, ychen2002@163.com

as the electrolyte, which has successfully achieved the integrated combination of optical modulation and energy storage [10]. However, due to the redox potential of $Al^{3+}$ (−1.66 V vs. standard hydrogen electrode (SHE)) being significantly lower than that of $H^+$, it proves challenging to efficiently reduce $Al^{3+}$ back onto the Al anode within the commonly used aqueous electrolyte. Consequently, during the coloring/bleaching (or charging/discharging) cycles, the Al electrode undergoes continuous oxidation and consumption, leading to high polarization and a shortened lifetime [11, 12]. Subsequently, Li et al. proposed the utilization of a Zn anode with a low redox potential (−0.76 V vs. SHE) and excellent stability in water to construct the Zn||tungsten oxide ECBs [13, 14]. In Zn||tungsten oxide ECBs, the use of a simple $Zn^{2+}$ cation electrolyte limits the capacity, switching speed, and optical contrast due to poor kinetic performance [15, 16]. In contrast, $Al^{3+}$, with its trivalence and small ionic radius (0.53 Å), serves as an effective charge carrier, enabling fast switching speeds, high optical contrast, and enhanced stability for tungsten oxide electrochromic electrodes. Consequently, a mixed $Zn^{2+}/Al^{3+}$ cation electrolyte is advantageous for developing stable, high-performance tungsten oxide-based electrochromic devices [16, 17]. However, ECBs constructed using Zn metal as the anode still face significant challenges that hinder the utilization of tungsten oxide-based ECBs. During the discharge process, due to the reduction of tungsten oxide, the discharge voltage rapidly decreases. The discharge plateau of the Zn-tungsten oxide ECBs occurs near 0.2 V, resulting in low power density and diminished practical applicability [14, 16]. Therefore, constructing ECBs with high capacity, especially high power density, holds crucial significance. Considering the chemical characteristics of tungsten oxide, the redox potential ($\Phi$ ($W^{6+}/W^{5+}$) = 0.3 V) is relatively low, making it more suitable as an anode material in the full battery system [10]. A novel approach is to explore a cathode material with a high redox potential as a counter electrode, using tungsten oxide as the anode to construct a new ECB system. This strategy holds promise for increasing the discharge voltage and significantly improving the energy density of $WO_3$-based ECBs.

In this study, a novel ECB was developed using acid-modified graphite foil (AGF) as the cathode, $WO_3$ as the anode, and hybrid $Zn^{2+}/Al^{3+}$ electrolyte (3 M $Zn(OTF)_2$ + 1 M $Al(OTF)_3$, OTF refers to the trifluoromethanesulfonate anion). The AGF offers advantages, such as high ion storage capacity, fast kinetics, and a high electrode potential, ensuring the $WO_3$||AGF ECB achieves a high discharge voltage and large capacity. The prepared $WO_3$||AGF ECB exhibits outstanding electrochromic performance, including an optical modulation of 80.9%, fast response time, excellent cycling stability, and superior optical memory effect. Additionally, it delivers a stable discharge capacity of up to 315.6 mAh·m$^{-2}$ at a charge–discharge density of 0.5 mA·cm$^{-2}$. This work proposes a new strategy for designing more compatible electrode material systems to achieve ECBs with higher energy and power densities, providing fresh insights for advancing the development of ECBs.

## 2 Results and discussion

$WO_3$ is one of the most widely used inorganic electrochromic materials due to its high optical modulation, rapid response time, and excellent cycling stability [18]. In this study, $WO_3$ was prepared using the magnetron sputtering method, which offers benefits, such as uniform film deposition, strong adhesion, and easily controllable thickness [19, 20]. The broad hump around 26° in the X-ray diffraction (XRD) pattern (Fig. 1(a)) confirms its amorphous structure, avoiding slow crystalline phase transitions, enhancing optical modulation and response speed [21, 22]. X-ray photoelectron spectroscopy (XPS) analysis further confirmed that the magnetron-sputtered film is $WO_3$. Figure S1 in the Electronic Supplementary Material (ESM) shows the full XPS spectrum of the sputtered $WO_3$, where only W, O, and a small amount of C are detected, with no other impurity signals, thereby confirming the successful synthesis of $WO_3$. Scanning electron microscopy (SEM) images reveal particles of about 250 nm with abundant voids and gaps (Fig. 1(b)), which facilitate the transport of electrolyte ions. The thickness of $WO_3$ has significantly impacted its electrochemical and electrochromic performance. In this study, $WO_3$ films with a uniform thickness of 400 nm were prepared under identical conditions (Fig. S2 and Table S1 in the ESM). Figure 1(c) presents the cyclic voltammetry (CV) curve of $WO_3$ in a three-electrode system, showing the anodic redox behavior within a voltage range of −0.6 to 0.2 V vs. Ag/AgCl. It exhibits good redox reversibility; however, the redox potential is relatively low, making it unsuitable for use as a battery cathode. The Dunn method (Eqs. (1) and (2)) [23] was employed to investigate the electrochemical kinetics of $WO_3$.

$$i = av^b \tag{1}$$

$$i = k_1 v + k_2 v^{0.5} \tag{2}$$

where $a$ and $b$ are adjustable parameters describing the relationship between the peak current ($i$) and the scan rate ($v$). The value of $b$ is used to determine the charge storage mechanism: $b$ = 0.5 indicates a diffusion-controlled process associated with ion intercalation, while $b$ = 1.0 corresponds to a surface-controlled capacitive process. $k_1$ and $k_2$ are constants at a given potential that separate the current response into capacitive ($k_1 v$) and diffusion-controlled ($k_2 v^{0.5}$) contributions. By plotting the logarithm of $i$ versus $v$, the fitted $b$-value for the oxidation peak was determined to be 0.9 (Fig. S3(a) in the ESM), indicating that the electrochemical behavior of $WO_3$ involves a combination of capacitive and diffusion-controlled processes [24]. Furthermore, the pseudocapacitive contributions at different scan rates were summarized in Fig. 1(d) and Fig. S3(b) in the ESM. As the scan rate increased from 1 to 6 mV·s$^{-1}$, the capacitive contribution rose from 65.0% to 91.0%, indicating that the $WO_3$ retains significant capacitive behavior at higher scan rates, which is crucial for enhancing its high-rate performance. This behavior is largely attributed to the rapid ion transport capability of the magnetron sputtered $WO_3$ [25], which enables fast electrochemical reactions and excellent rate performance (Fig. S4 in the ESM). However, in a conventional Zn||$WO_3$ battery, where Zn foil is used as the anode and $WO_3$ as the cathode, the discharge potential is relatively low, significantly constraining the performance of $WO_3$-based ECBs [16]. Therefore, $WO_3$ is more suitable as an anode material in full-cell systems. A novel approach would be to explore high-redox-potential cathode materials as the counter electrode while using $WO_3$ as the anode. This new ECB system could enhance the discharge voltage of $WO_3$-based ECBs.

Graphite foil (GF), made from graphite material, is characterized by excellent conductivity, strong chemical stability, structural integrity, and a wide electrochemical window [26, 27]. These properties make it a promising candidate for use as the cathode

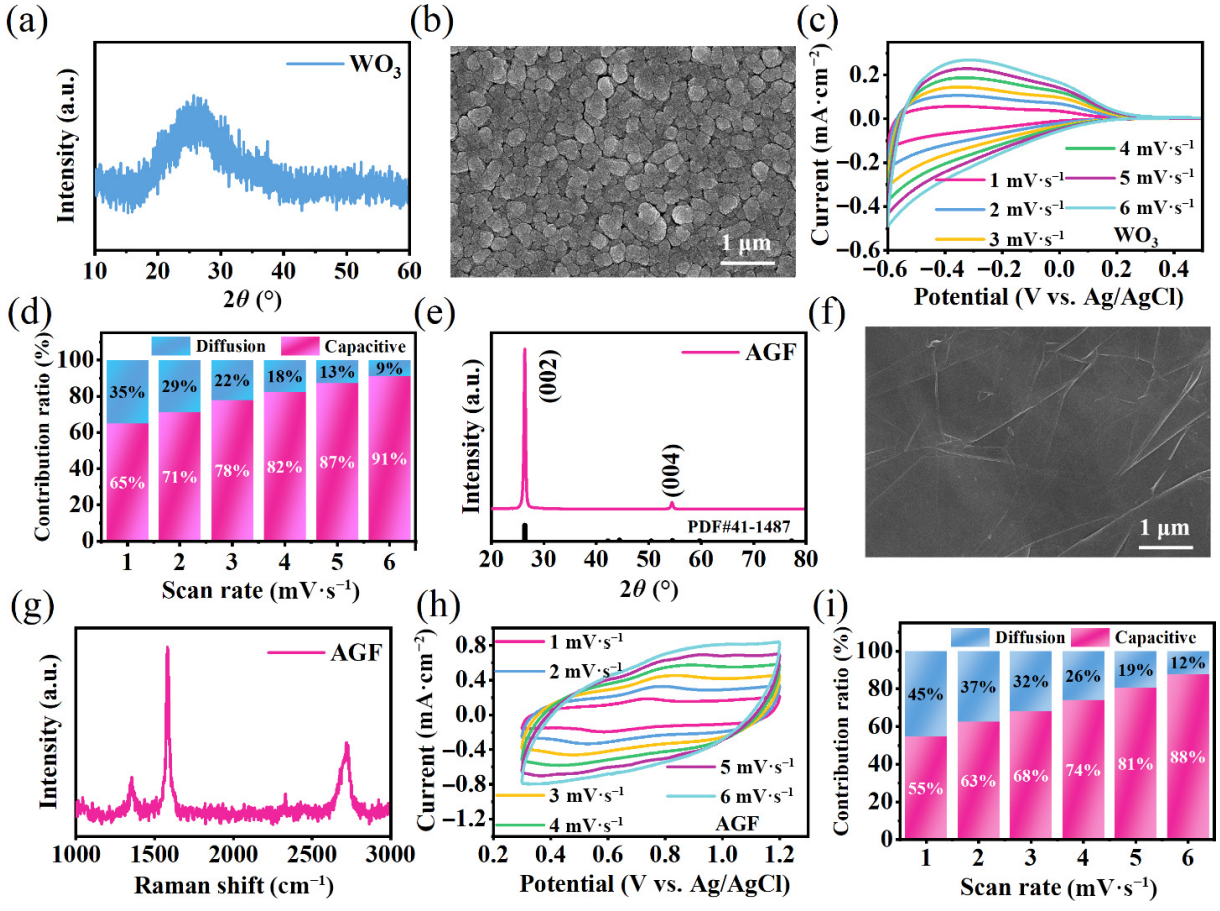


**Figure 1** (a) XRD pattern and (b) surface SEM of $WO_3$. (c) CV curves and (d) capacitive contribution of the $WO_3$ films. (e) XRD pattern, (f) surface SEM, and (g) Raman pattern of AGF. (h) CV curves and (i) capacitive contribution of the AGF.

material in $WO_3$-based batteries. Here, commercially available GF was selected (optical image shown in Fig. S5 in the ESM). To further enhance the oxidation potential window and ion transport properties of the GF, acid oxidation treatment was performed by soaking it in 10 wt.% $H_2SO_4$ solution for 2 h. The resulting AGF was then used as the cathode material in $WO_3$-based ECBs. XRD analysis revealed that AGF exhibits narrow and sharp characteristic peaks at 26.4° and 54.5° (Fig. 1(e)), corresponding to the graphite reference pattern (PDF#41-1487) [28, 29], indicating a high degree of graphitization in the AGF. SEM image shows that AGF consists of multiple layers of stacked graphite (Fig. 1(f)), consistent with the results from transmission electron microscopy (TEM) analysis (Figs. S6(a) and S6(b) in the ESM). Furthermore, high-resolution TEM (HRTEM) images (Fig. S6(c) in the ESM) demonstrate a lattice spacing of 0.33 nm, corresponding to the (002) plane of graphite [30, 31]. Additionally, selected area electron diffraction (SAED) analysis confirms the presence of multilayer graphite diffraction pattern (Fig. S6(d) in the ESM), reflecting the highly ordered structure of the AGF. The effects of acid treatment on the structure and surface chemistry of GF were systematically investigated using Raman spectroscopy, Fourier transform infrared spectroscopy (FTIR), and XPS. Raman spectra (Fig. 1(g) and Fig. S7 in the ESM) revealed that the intensity ratio of the D and G bands ($I_D/I_G$) increased from 0.1 (GF) to 0.3 (AGF), indicating the introduction of more structural defects and functional groups after acid treatment [32]. FTIR (Fig. S8 in the ESM) and XPS (Fig. S9 in the ESM) analyses further confirmed the incorporation of abundant oxygen-containing functional groups, such as hydroxyl (C–OH) and carboxyl (–COOH), on the AGF surface [33]. The overall oxygen content increased from 5.8% to 10.4%. These results demonstrate that acid treatment effectively modifies the defect structure and surface functionalities of graphite, thereby enhancing its electrochemical activity. Further, the electrochemical properties of AGF were evaluated by CV curves in a three-electrode system with an Ag/AgCl reference electrode (Fig. 1(h)), which reveal an electrochemical active window in the range of 0.4–1.2 V. Compared to $WO_3$, AGF exhibits a much higher electrochemical active window, indicating its potential as a more suitable cathode material to pair with $WO_3$. Additionally, AGF shows distinct redox peaks at 0.6 and 0.7 V, with a larger CV loop area compared to untreated GF (Fig. S10 in the ESM). This improvement is mainly attributed to oxygen-containing functional groups introduced during the acid treatment, demonstrating a significant enhancement in the electrochemical performance of the graphite foil after acid treatment [33]. As the scan rate increases from 1 to 6 mV·s$^{-1}$, the capacitive contribution of the AGF electrode rises from 55% to 88% (Fig. 1(i) and Fig. S11 in the ESM). AGF displays excellent pseudocapacitive ion storage behavior, contributing to better rate performance. These results indicate that AGF, with its wide electrochemical activity window, holds promise as a cathode material for $WO_3$-based ECBs, offering higher discharge voltage, energy density, and rate capability.

The $WO_3$||AGF ECB introduces a novel system with $WO_3$ as the anode and AGF as the cathode, using a hybrid electrolyte of 3 M

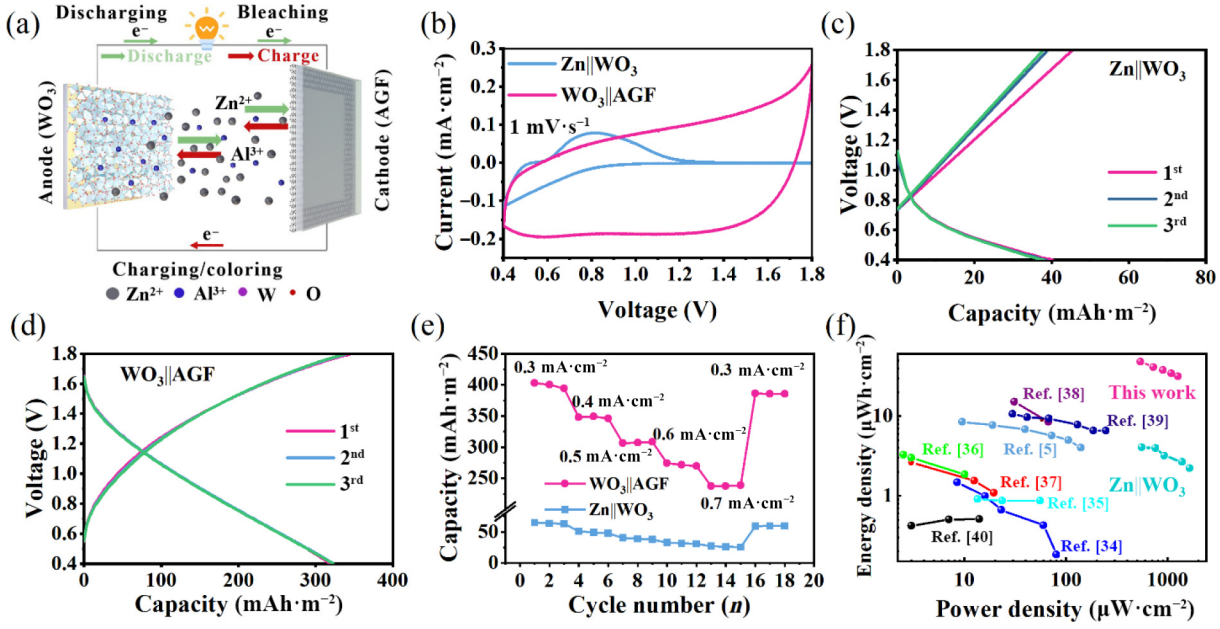


**Figure 2** (a) Schematic of the $WO_3$||AGF ECB. (b) CV curves of $WO_3$||AGF and Zn||$WO_3$. ((c) and (d)) GCD profiles of (c) Zn||$WO_3$ and (d) AGF||$WO_3$ at 0.5 mA·cm$^{-2}$. (e) Rate performance of $WO_3$||AGF and Zn||$WO_3$. (f) Ragone plot of $WO_3$||AGF and other reported ECBs.

$Zn(OTF)_2$ + 1 M $Al(OTF)_3$ (Fig. 2(a)). For comparison, a conventional Zn||$WO_3$ ECB was fabricated using the same $WO_3$ film electrode and electrolyte, with $WO_3$ acting as the cathode. Figure 2(b) presents the CV curves of the 3 cm × 3 cm $WO_3$||AGF and Zn||$WO_3$ ECBs. The Zn||$WO_3$ ECB shows two anodic peaks at 0.5 and 0.8 V, with no distinct cathodic peak, indicating a multi-step de-intercalation and a single-step intercalation process [16]. The CV area enclosed by $WO_3$||AGF ECB is significantly larger than that of Zn||$WO_3$ ECB, indicating a much higher charge storage capacity, which is further confirmed by the galvanostatic charge–discharge (GCD) test results. At a charge–discharge current density of 0.5 mA·cm$^{-2}$, the $WO_3$||AGF ECB achieved a stable, high discharge capacity of 315.6 mAh·m$^{-2}$, which is 7.8 times greater than the discharge capacity of the conventional Zn||$WO_3$ ECB (40.4 mAh·m$^{-2}$) (Figs. 2(c) and 2(d)). The complete discharge capability is achieved due to the well-matched pairing of the $WO_3$ anode and the AGF cathode. Additionally, the $WO_3$||AGF ECB exhibits excellent rate capability across various current densities (0.3–0.7 mA·cm$^{-2}$), achieving high discharge capacities of 376.4, 340.4, 315.6, 290.0, and 265.6 mAh·m$^{-2}$, respectively. These values are far superior to the reversible capacities of the Zn||$WO_3$ ECB under the same current densities (64.8, 50.8, 40.4, 33.2, and 27.2 mAh·m$^{-2}$). Even when the current density is reduced back to 0.3 mA·cm$^{-2}$ during rate cycling, the $WO_3$||AGF ECB recovers a reversible capacity of 361.2 mAh·m$^{-2}$, demonstrating excellent rate stability (Fig. 2(e)). At a power density of 1 mW·cm$^{-2}$, the energy density of the new $WO_3$||AGF ECB is 11.8 times that of the Zn||$WO_3$ ECB, far exceeding the performance of currently reported electrochromic energy storage devices (Fig. 2(f)) [5, 34–40]. The ability of $WO_3$ to fully discharge as an anode material is largely due to AGF's wide electrochemical potential window and fast ion transport kinetics. *Ex situ* Raman results show that, during charging, the characteristic peaks at 1355 cm$^{-1}$ (D band) and 2719 cm$^{-1}$ (2D band) gradually shift to lower frequencies, while during discharge, they shift back to higher frequencies, eventually returning to their initial positions. However, the characteristic peak at 1583 cm$^{-1}$ (G band) remains unchanged during the charge–discharge process (Fig. S12 in the ESM). This indicates that the defect-related D band in AGF plays a key role in energy storage while enabling fast, reversible, and efficient charge transfer [29].

The $WO_3$||AGF ECB not only exhibits outstanding electrochemical energy storage performance, such as a high discharge voltage and large energy storage capacity, but also demonstrates excellent electrochromic properties, including high optical modulation, fast response time, high coloration efficiency (CE), excellent cycling stability, and a strong open-circuit memory effect. Figure 3(a) shows the transmittance curves of the $WO_3$||AGF and Zn||$WO_3$ devices in the colored state (1.8 V for $WO_3$||AGF, 0.1 V for Zn||$WO_3$) and bleached state (0 V for $WO_3$||AGF, 1.2 V for Zn||$WO_3$). The $WO_3$||AGF ECB exhibits a transmittance of 81.2% in the bleached state and 0.3% in the colored state at 700 nm, resulting in an impressive optical modulation of 80.9%, which is slightly higher than the 78.4% optical modulation observed for the Zn||$WO_3$ ECB. XPS was used to analyze the intrinsic mechanism of the coloring reaction in $WO_3$ and AGF. In the pristine sample's XPS spectrum, the W 4f orbitals can be deconvoluted into five characteristic peaks, corresponding to $W^{6+}$ ($4f_{7/2}$ and $4f_{5/2}$), $W^{5+}$ ($4f_{7/2}$ and $4f_{5/2}$), and $W^{5+}$ $5p_{3/2}$ (Fig. S13(a) in the ESM). The presence of $W^{5+}$ may be attributed to the incomplete oxidation of $WO_3$ films prepared at room temperature, resulting in trace amounts of $W^{5+}$ in the sample [41]. In the colored state of $WO_3$, the XPS spectrum shows the valence states of $W^{6+}$, $W^{5+}$, and $W^{4+}$ (Fig. S13(b) in the ESM), which are primarily attributed to the reduction of W induced by ion insertion [42, 43]. By comparing the full spectra of $WO_3$ before and after coloring, the XPS results of the colored $WO_3$ anode show the detection of Al (Figs. S13(c) and S13(d) in the ESM), indicating that the reduction of $W^{6+}$ is caused by the insertion of $Al^{3+}$, which is consistent with previous reports on $Zn^{2+}$/$Al^{3+}$ mixed electrolytes [16, 17]. Furthermore, the presence of Zn 2p and Al 2p signals on AGF in the bleached state of $WO_3$, which disappear in the colored state (Fig. S14 in the ESM), suggests that both $Zn^{2+}$ and $Al^{3+}$ ions are involved in the electrochemical processes of AGF without significant ion selectivity.

The response time refers to the time required to reach 90% of the

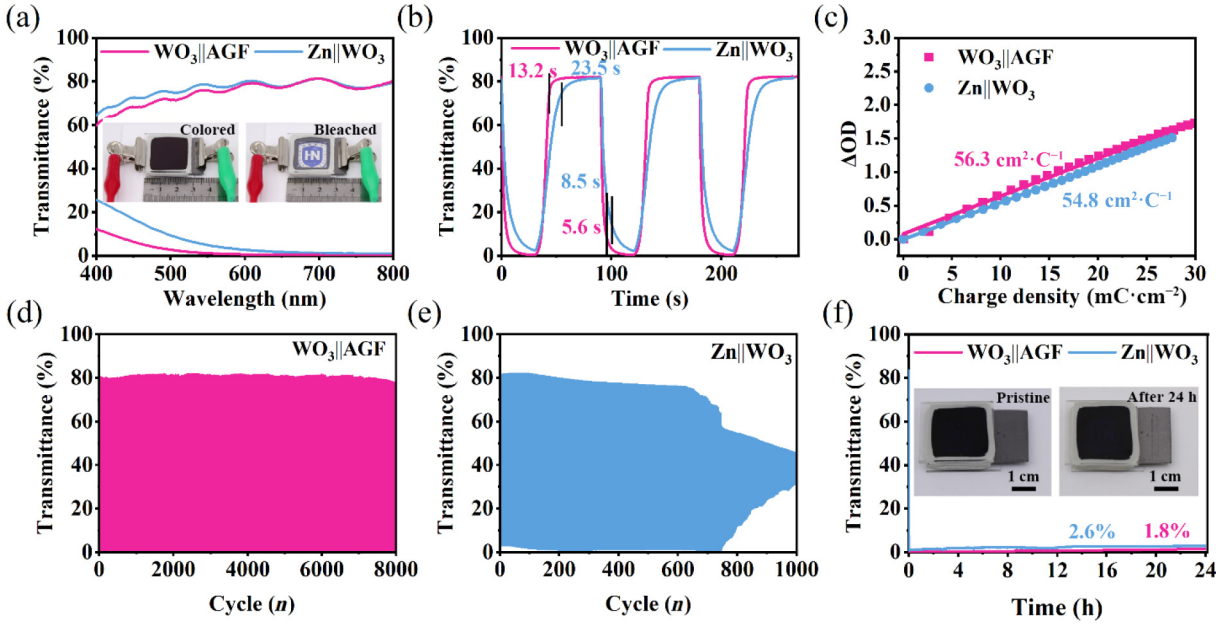


**Figure 3** (a) Transmission spectra in the visible range. Inset photos demonstrate colored and bleached states of the 3 cm × 3 cm $WO_3$||AGF ECB. (b) Switching time and (c) ΔOD (700 nm) versus charge density of $WO_3$||AGF and Zn||$WO_3$ ECBs. ((d) and (e)) Cyclic stability of (d) $WO_3$||AGF and (e) Zn||$WO_3$ ECBs. (f) Optical transmittance monitoring of colored 3 cm × 3 cm $WO_3$||AGF and Zn||$WO_3$ ECBs at 700 nm under open-circuit conditions, with inset of $WO_3$||AGF ECB in its initial and 24 h open-circuit colored states.

optical modulation during the coloring and bleaching processes. As shown in Fig. 3(b), the $WO_3$||AGF ECB exhibits coloring/bleaching times of 5.6/13.2 s, which are shorter than the 8.5/23.5 s observed in the Zn||$WO_3$ ECB. The significantly reduced response time of the $WO_3$||AGF electrochromic device is primarily due to the excellent ion storage pseudocapacitive behavior of AGF and its rapid kinetic processes. Coloring/bleaching tests on the $WO_3$||GF electrochromic device, assembled with GF, revealed that after applying the same bleaching voltage following the coloring process, the device could not completely return to its original bleached state, achieving only a 34.7% optical modulation (Fig. S15 in the ESM). The oxygen-containing functional groups introduced during acid treatment enhance the oxidative capacity, ensuring a faster bleaching time and higher transparency in the bleached state for the $WO_3$||AGF device. CE is also an important parameter for evaluating electrochromic devices. The calculation equation [17] is as Eq. (3)

$$\mathrm{CE} = \frac{\Delta \mathrm{OD}}{\Delta Q} = \lg\left(\frac{T_\mathrm{b}}{T_\mathrm{c}}\right)/\Delta Q \quad (3)$$

where ΔOD represents the variation of optical density, $T_\mathrm{b}$ and $T_\mathrm{c}$ represent the transmittance in the bleached and colored states, respectively. $\Delta Q$ represents the charge density obtained by integrating the current–time curve during the coloring process. The calculated CE for the $WO_3$||AGF ECB is 56.3 $cm^2 \cdot C^{-1}$, comparable to the 54.8 $cm^2 \cdot C^{-1}$ of the Zn||$WO_3$ ECB (Fig. 3(c)), demonstrating the high energy efficiency of the $WO_3$ electrode. Figures 3(d) and 3(e) show the transmittance variation curves for the $WO_3$||AGF and Zn||$WO_3$ ECBs under alternating coloring (30 s) and bleaching (60 s) voltages. The coloring/bleaching voltages for the $WO_3$||AGF device were 1.8/0 V, while for the Zn||$WO_3$ device, they were 0.1/1.2 V. The Zn||$WO_3$ ECB exhibited an optical modulation of only 13.6% and a retention rate of just 17.3% after 1000 cycles. Additionally, during cycling, the transmittance in the bleached state of the Zn||$WO_3$ ECB continuously decreased. This degradation in device performance is primarily due to side reactions at the Zn anode, including Zn dendrite formation, passivation, during charge–discharge processes [44, 45]. In contrast, after 8000 cycles, the $WO_3$||AGF ECB maintained an optical modulation of 76.4% with a retention rate of 94.4%. Characterization of the AGF and Zn foil after 1000 coloring/bleaching cycles revealed significant differences between the two devices. The surface morphology (Fig. S16 in the ESM) and composition (Fig. S17 in the ESM) of AGF in the $WO_3$||AGF device remained stable, while the Zn foil in the Zn||$WO_3$ device exhibited significant Zn dendrite formation (Fig. S18 in the ESM) and by-products, including $Zn_x(OTF)_y(OH)_{2x-y} \cdot nH_2O$ and ZnO [46, 47] (Fig. S19 in the ESM), which hinder reversible ion transport. These by-products altered the potential applied to the $WO_3$ electrode, reducing cycling stability. Material characterization was also conducted on the $WO_3$ films in the $WO_3$||AGF and Zn||$WO_3$ devices after 1000 cycles. Cracks with widths of ~ 50 and ~ 70 nm were observed in the $WO_3$ films of the $WO_3$||AGF and Zn||$WO_3$ devices, respectively. While the particle size of $WO_3$ in the $WO_3$||AGF device remained unchanged, it decreased to 190 nm in the Zn||$WO_3$ device (Fig. S20 in the ESM). XRD analysis revealed stable patterns for $WO_3$ at bleached state in the $WO_3$||AGF device after 1000 coloring/bleaching cycles, whereas $WO_3$ in the Zn||$WO_3$ device exhibited $ZnWO_4$ peaks [44] (Fig. S21 in the ESM), indicating the formation of inactive by-products. This was attributed to Zn dendrites and by-products altering the potential of the $WO_3$ electrode, leading to partial $WO_3$ dissolution and $ZnWO_4$ formation. When the failed Zn||$WO_3$ electrochromic device was repaired by replacing the Zn foil with a new one, its coloring functionality was restored. However, the transmittance in the bleached state was reduced (Fig. S22 in the ESM) due to the presence of inactive $ZnWO_4$. The open-circuit memory effect refers to a material's ability to maintain its current optical state after the power supply is disconnected [48]. Figure 3(f) illustrates the change in transmittance of the electrochromic device over 24 h in the

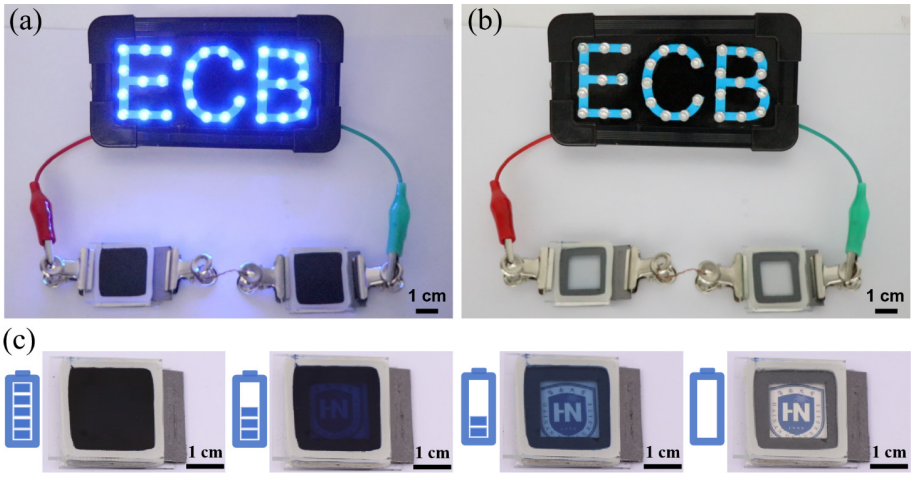


**Figure 4** (a) Two series-connected $WO_3$||AGF ECBs powering a display in a fully charged state. (b) In a fully discharged state. (c) Photos corresponding to different residual power levels (100%, 60%, 40%, and 0%).

colored state without energy input. The transmittance of the $WO_3$||AGF device increased from 0.1% to 1.5%, showing only a 1.8% rise, with no visible change to the naked eye, demonstrating excellent open-circuit memory performance. This could be attributed to the reduced presence of free water molecules in the 3 M $Zn(OTF)_2$ + 1 M $Al(OTF)_3$ mixed electrolyte. Moreover, the high charge density and small size of $Al^{3+}$ allow it to form more stable electrostatic interactions with tungsten oxide. These factors work together to suppress the dissolution of embedded $Al^{3+}$ ions [17, 49, 50]. Benefiting from the high ion storage capacity, fast kinetics, and high electrode potential of AGF, the $WO_3$||AGF ECB exhibits excellent overall performance. Table S2 in the ESM compares its key parameters with reported ECBs [9, 16, 17, 39], showing superior optical modulation, capacity, and cycling stability, highlighting its strong potential for practical applications. Achieving uniform electrochromic modulation across large areas has long been a challenge for ECBs. The use of opaque frames as counter electrodes can affect the performance and uniformity of electrochromic devices, especially in larger-scale applications. The extent of this impact is closely related to the ion transport dynamics of the frame electrode. AGF, which possesses excellent ion insertion/extraction kinetics, effectively mitigates this issue, ensuring that the device maintains good electrochromic performance under normal operating conditions. For the 10 cm × 10 cm $WO_3$||AGF ECB we fabricated, the ratio of the graphite foil frame width to the device size was 1:10, which allows for uniform coloration in the colored state (Fig. S23 in the ESM).

Due to the high energy density and excellent electrochromic performance of the $WO_3$||AGF ECB, the device is capable of powering a 0.8 V light-emitting diode (LED), showcasing its potential for practical applications as an electrochromic energy storage device (Fig. S24 in the ESM). Figure 4(a) shows a photograph of the fully charged $WO_3$||AGF ECB, which successfully powers a display consisting of 30 LEDs. As the stored energy depletes, the device transitions from black to transparent (Fig. 4(b)). Figure S25 in the ESM illustrates the corresponding changes in optical transmittance during charging and discharging cycles. During charging, the transmittance gradually decreases, reaching as low as 0.1% when fully charged. During discharge, the transmittance increases progressively, reaching 80.6% when fully depleted. The color state of the ECB allows us to visually estimate the remaining charge of the energy storage device (Fig. 4(c)). These results demonstrate that the $WO_3$||AGF ECB not only enables reversible color changes but also functions as a visual energy storage device capable of powering low-power electronics. This offers a new approach for developing next-generation energy-saving and multifunctional smart windows.

## 3 Conclusions

In this work, a novel $WO_3$||AGF ECB was developed using AGF as the cathode, $WO_3$ as the anode, and a hybrid $Zn^{2+}/Al^{3+}$ electrolyte. The AGF electrode demonstrates high ion storage capacity, fast kinetics, and a high electrode potential, ensuring both a high discharge voltage and full utilization of the storage capacity of the $WO_3$||AGF ECB. At a charge–discharge density of 0.5 $mA{\cdot}cm^{-2}$, the $WO_3$||AGF ECB achieved a discharge capacity of 315.6 $mAh{\cdot}m^{-2}$, which is 7.8 times higher than that of a conventional Zn||$WO_3$ ECB. At a power density of 1 $mW{\cdot}cm^{-2}$, the energy density of the $WO_3$||AGF ECB was 11.8 times that of the Zn||$WO_3$ ECB. Additionally, the $WO_3$||AGF ECB exhibited excellent electrochromic performance, including an optical modulation rate of 80.9%, fast coloring/bleaching switching times (5.6/13.2 s), high cycling stability (with 94.4% retention after 8000 cycles), and an outstanding open-circuit memory effect (with an optical transmittance increase of only 1.8% after 24 h). As a demonstration, the $WO_3$||AGF ECB was able to power a display composed of 30 LEDs, with the remaining capacity visually trackable through the color change of the device. This work offers a new approach for constructing high energy density and high power density smart ECBs by designing more compatible electrode material systems.

**Electronic Supplementary Material**: Supplementary material (experimental section, SEM and XPS spectra of $WO_3$, TEM images of AGF, CV curves of $WO_3$ and GF, rate capability of $WO_3$ electrode, *ex situ* Raman spectra of AGF, electro-chromic data, digital photos of the AGF and ECDs, SEM images of AGF, Zn foil and $WO_3$ before and after cycling, optical images of a LED powered by the $WO_3$||AGF ECB, and optical transmittance of $WO_3$||AGF ECB during charge/discharge cycles) is available in the online version of this article at https://doi.org/10.26599/NR.2025.94907799.

## Data availability

All data needed to support the conclusions in the paper are presented in the manuscript and the Electronic Supplementary Material. Additional data related to this paper may be requested from the corresponding author upon request.

## Acknowledgements

This work is financially supported by the National Natural Science Foundation of China (Nos. 52462040 and 52172299), Hainan Province "Nanhai New Star" Science and Technology Innovation Talent Platform Program (No. NHXXRCXM202304), Innovation Team of Universities of Guangdong Province (No. 2022KCXTD030), the "Targeted Technology Innovation Initiative" Project at the Foshan National Institute of Innovation (No. JBGS2024002), the Postdoctoral Fellowship Program of CPSF (No. GZB20250029), and the China Postdoctoral Science Foundation (No. 2025M770830). S. C. would like to acknowledge the support from the External Cooperation Program of the Chinese Academy of Sciences (No. 320GJHZ2023011MI), Suzhou Industrial Science and Technology Program (No. SYC2022036), and High-end Talents Program of Jiangxi Province (No. jxsq2023101113).

## Declaration of competing interest

All the contributing authors report no conflict of interests in this work.

## Author contribution statement

Y. Y. C.: Writing manuscript, experimental design, data curation, project administration. J. B. W.: Writing manuscript, data curation, project administration. C. Y. Z.: Project administration, data curation, validation. X. Q. T.: Project administration, data curation, funding acquisition. L. C.: Project administration. Z. X. T.: Project administration. D. L.: Validation, project administration. Y. C.: Funding acquisition, project administration. C. H. W.: Project administration. S. C.: Project administration, funding acquisition. Z. G. Z.: Project administration, funding acquisition. Z. W.: Writing manuscript, project administration, funding acquisition, validation. All the authors have approved the final manuscript.

## Use of AI statement

None.

## References

[1] Pathak, D. K.; Moon, H. C. Recent progress in electrochromic energy storage materials and devices: A minireview. *Mater. Horiz.* **2022**, *9*, 2949–2975.

[2] Zhao, F. F.; Wang, B.; Zhang, W.; Cao, S.; Liu, L. H.; Elezzabi, A. Y.; Li, H. Z.; Yu, W. W. Counterbalancing the interplay between electrochromism and energy storage for efficient electrochromic devices. *Mater. Today* **2023**, *66*, 431–447.

[3] Wang, Z.; Wang, X. Y.; Cong, S.; Geng, F. X.; Zhao, Z. G. Fusing electrochromic technology with other advanced technologies: A new roadmap for future development. *Mater. Sci. Eng. R Rep.* **2020**, *140*, 100524.

[4] Ma, Q.; Chen, J. X.; Zhang, H.; Su, Y. W.; Jiang, Y. J.; Dong, S. J. Dual-function self-powered electrochromic batteries with energy storage and display enabled by potential difference. *ACS Energy Lett.* **2023**, *8*, 306–313.

[5] Wang, B.; Cui, M. W.; Gao, Y. F.; Jiang, F. Y.; Du, W.; Gao, F.; Kang, L. T.; Zhi, C. Y.; Luo, H. J. A long-life battery-type electrochromic window with remarkable energy storage ability. *Solar RRL* **2020**, *4*, 1900425.

[6] Liu, Q. B.; Ou, X.; Niu, Y. J.; Li, L. G.; Xing, D. D.; Zhou, Y. J.; Yan, F. Flexible Zn-ion electrochromic batteries with multiple-color variations. *Angew. Chem., Int. Ed.* **2024**, *63*, e202317944.

[7] Granqvist, C. G. Electrochromic tungsten oxide films: Review of progress 1993–1998. *Solar Energy Mater. Solar Cells* **2000**, *60*, 201–262.

[8] Gu, C.; Jia, A. B.; Zhang, Y. M.; Zhang, S. X. A. Emerging electrochromic materials and devices for future displays. *Chem. Rev.* **2022**, *122*, 14679–14721.

[9] Roy, R.; Ganesha, M. K.; Dutta, P.; Pal, D.; Singh, A. K. High-performance aqueous electrochromic battery for smart window application: Mechanistic insights of Al-ion (de)intercalation kinetics in thickness-optimized $WO_3$. *ACS Appl. Energy Mater.* **2023**, *6*, 11683–11693.

[10] Zhao, J. X.; Tian, Y. Y.; Wang, Z.; Cong, S.; Zhou, D.; Zhang, Q. Z.; Yang, M.; Zhang, W. K.; Geng, F. X.; Zhao, Z. G. Trace $H_2O_2$ - assisted high - capacity tungsten oxide electrochromic batteries with ultrafast charging in seconds. *Angew. Chem.* **2016**, *128*, 7277–7281.

[11] Wang, J. M.; Zhang, L.; Yu, L.; Jiao, Z. H.; Xie, H. Q.; Lou, X. W.; Sun, X. W. A Bi-functional device for self-powered electrochromic window and self-rechargeable transparent battery applications. *Nat. Commun.* **2014**, *5*, 4921.

[12] Sun, S. B.; Tang, C. J.; Jiang, Y. C.; Wang, D. S.; Chang, X. T.; Lei, Y. H.; Wang, N. N.; Zhu, Y. Q. Flexible and rechargeable electrochromic aluminium-ion battery based on tungsten oxide film electrode. *Solar Energy Mater. Solar Cells* **2020**, *207*, 110332.

[13] Chen, J. W.; Xu, B.; Zhang, Y. X.; Zhang, W.; Wang, H. L.; Elezzabi, A. Y.; Liu, L. H.; Yu, W. W.; Li, H. Z. The birth of zinc anode-based electrochromic devices. *Appl. Phys. Rev.* **2024**, *11*, 011316.

[14] Li, H. Z.; McRae, L.; Firby, C. J.; Elezzabi, A. Y. Rechargeable aqueous electrochromic batteries utilizing Ti-substituted tungsten molybdenum oxide based $Zn^{2+}$ ion intercalation cathodes. *Adv. Mater.* **2019**, *31*, 1807065.

[15] Weng, S. C.; Cao, Z. H.; Song, K. R.; Chen, W. T.; Jiang, R.; Rogachev, A. A.; Yarmolenko, M. A.; Zhou, J. M.; Zhang, H. L. Constructing an $Al^{3+}/Zn^{2+}$-based solid electrolyte interphase to enable extraordinarily stable $Al^{3+}$-based electrochromic devices. *ACS Appl. Mater. Interfaces* **2024**, *16*, 18164–18172.

[16] Li, H. Z.; Firby, C. J.; Elezzabi, A. Y. Rechargeable aqueous hybrid $Zn^{2+}/Al^{3+}$ electrochromic batteries. *Joule* **2019**, *3*, 2268–2278.

[17] Wu, C.; Shi, H. S.; Zhao, L. Q.; Chen, X.; Zhang, X. S.; Zhang, C.; Yu, J. M.; Lv, Y. J.; Wei, R.; Gao, T. Y. et al. High-performance aqueous $Zn^{2+}/Al^{3+}$ electrochromic batteries based on niobium tungsten oxides. *Adv. Funct. Mater.* **2023**, *33*, 2214886.

[18] Arslan, M.; Firat, Y. E.; Tokgöz, S. R.; Peksoz, A. Fast electrochromic response and high coloration efficiency of Al-doped $WO_3$ thin films for smart window applications. *Ceram. Int.* **2021**, *47*, 32570–32578.

[19] Tajima, K.; Watanabe, H.; Nishino, M.; Kawamoto, T. Electrochromic properties of $WO_3$ thin films fabricated by magnetron sputtering, ion plating, and spin coating: A comparative investigation. *J. Ceram. Soc. Jpn.* **2020**, *128*, 381–386.

[20] Limwichean, S.; Eiamchai, P.; Ponchio, C.; Kasayapanand, N.; Horprathum, M. Comparative investigations of DCMS/HiPIMS reactively sputtered $WO_3$ thin films for photo-electrochemical efficiency enhancements. *Vacuum* **2021**, *185*, 109978.

[21] Wu, Q.; Wang, X. Y.; Sun, P. Y.; Wang, Z.; Chen, J.; Chen, Z. G.; Song, G.; Liu, C. L.; Mu, X. Y.; Cong, S. et al. Electrochromic metamaterials of metal-dielectric stacks for multicolor displays with high color purity. *Nano Lett.* **2021**, *21*, 6891–6897.

[22] Zhang, S. L.; Peng, Y. T.; Zhao, J.; Fan, Z. J.; Ding, B.; Lee, J. Y.; Zhang, X. G.; Xuan, Y. M. Amorphous and porous tungsten oxide films for fast-switching dual-band electrochromic smart windows. *Adv. Opt. Mater.* **2023**, *11*, 2202115.

[23] Qin, L.; Zhu, S. H.; Cheng, C.; Wu, D. X.; Wang, G. Y.; Hou, L. R.; Yuan, C. Z. Single-crystal nano-subunits assembled accordion-shape $WNb_2O_8$ framework with high ionic/electronic conductivities towards Li-ion capacitors. *Small* **2022**, *18*, 2107987.
[24] Kim, J.; Inamdar, A. I.; Jo, Y.; Cho, S.; Ahmed, A. T. A.; Hou, B.; Cha, S.; Kim, T. G.; Kim, H.; Im, H. Nanofilament array embedded tungsten oxide for highly efficient electrochromic supercapacitor electrodes. *J. Mater. Chem. A* **2020**, *8*, 13459–13469.
[25] Han, Z. A.; Tong, M. Y.; Zhang, C. Y.; Guo, X. L.; Chen, Y. Y.; Chen, W.; Zhong, H. D.; Wan, J. B.; Cai, S. X.; Ma, Y. P. et al. Unlocking dual-band electrochromism with stacked structure of amorphous tungsten oxide and Prussian blue. *Solar Energy Mater. Solar Cells* **2024**, *273*, 112939.
[26] Munuera, J. M.; Paredes, J. I.; Villar-Rodil, S.; Martínez-Alonso, A.; Tascón, J. M. D. A simple strategy to improve the yield of graphene nanosheets in the anodic exfoliation of graphite foil. *Carbon* **2017**, *115*, 625–628.
[27] Cui, L. F.; Wang, X. P.; Chen, N.; Zhang, G. F.; Qu, L. T. A versatile graphene foil. *J. Mater. Chem. A* **2017**, *5*, 14508–14513.
[28] Li, Y. M.; Guo, Q.; Wu, Y.; Ying, D. F.; Yu, Y.; Chi, T. S.; Xia, S. J.; Zhou, X. F.; Liu, Z. P. Artificial graphite paper as a corrosion-resistant current collector for long-life lithium metal batteries. *Adv. Funct. Mater.* **2023**, *33*, 2214523.
[29] Kim, J.; Raj, M. R.; Lee, G. High-defect-density graphite for superior-performance aluminum-ion batteries with ultra-fast charging and stable long life. *Nano-Micro Lett.* **2021**, *13*, 171.
[30] Mu, Y. B.; Han, M. S.; Li, J. Y.; Liang, J. B.; Yu, J. Growing vertical graphene sheets on natural graphite for fast charging lithium-ion batteries. *Carbon* **2021**, *173*, 477–484.
[31] Li, L.; Liu, L. J.; Hu, Z.; Lu, Y.; Liu, Q. N.; Jin, S.; Zhang, Q.; Zhao, S.; Chou, S. L. Understanding high-rate $K^+$-solvent Co-intercalation in natural graphite for potassium-ion batteries. *Angew. Chem., Int. Ed.* **2020**, *59*, 12917–12924.
[32] Wang, Y.; Alsmeyer, D. C.; McCreery, R. L. Raman spectroscopy of carbon materials: Structural basis of observed spectra. *Chem. Mater.* **1990**, *2*, 557–563.
[33] Liu, Z. Y.; Wang, L. D.; Ma, G. Z.; Yuan, Y.; Jia, H.; Fei, W. D. A supercapacitor with ultrahigh volumetric capacitance produced by self-assembly of reduced graphene oxide through phosphoric acid treatment. *J. Mater. Chem. A* **2020**, *8*, 18933–18944.
[34] Wang, J. Q.; Liu, J.; Hu, M. M.; Zeng, J.; Mu, Y. B.; Guo, Y.; Yu, J.; Ma, X.; Qiu, Y. J.; Huang, Y. A flexible, electrochromic, rechargeable Zn//PPy battery with a short circuit chromatic warning function. *J. Mater. Chem. A* **2018**, *6*, 11113–11118.
[35] Bi, Z. J.; Li, X. M.; Chen, Y. B.; He, X. L.; Xu, X. K.; Gao, X. D. Large-scale multifunctional electrochromic-energy storage device based on tungsten trioxide monohydrate nanosheets and Prussian white. *ACS Appl. Mater. Interfaces* **2017**, *9*, 29872–29880.
[36] Zhai, Y. L.; Li, Y.; Zhang, H.; Yu, D. B.; Zhu, Z. J.; Sun, J. Z.; Dong, S. J. Self-rechargeable-battery-driven device for simultaneous electrochromic windows, ROS biosensing, and energy storage. *ACS Appl. Mater. Interfaces* **2019**, *11*, 28072–28077.
[37] Zhang, W.; Li, H. Z.; Al-Hussein, M.; Elezzabi, A. Y. Electrochromic battery displays with energy retrieval functions using solution-processable colloidal vanadium oxide nanoparticles. *Adv. Opt. Mater.* **2020**, *8*, 1901224.
[38] Eric, H.; Li, H. Z.; Adulhakem Y., E. Rechargeable $Zn^{2+}/Al^{3+}$ dual-ion electrochromic device with long life time utilizing dimethyl sulfoxide (DMSO)-nanocluster modified hydrogel electrolytes. *RSC Adv.* **2019**, *9*, 32047–32057.
[39] Tong, Z. Q.; Lian, R. Q.; Yang, R.; Kang, T. X.; Feng, J. R.; Shen, D.; Wu, Y.; Cui, X.; Wang, H.; Tang, Y. B. et al. An aqueous aluminum-ion electrochromic full battery with water-in-salt electrolyte for high-energy density. *Energy Storage Mater.* **2022**, *44*, 497–507.
[40] Zhai, Y. L.; Li, Y.; Zhu, Z. J.; Zhu, C. Z.; Du, D.; Lin, Y. H. Self-driven multicolor electrochromic energy storage windows powered by a "perpetual" rechargeable battery. *ACS Appl. Mater. Interfaces* **2019**, *11*, 48013–48020.
[41] Roy, R.; Mahendra, G.; Singh, A. K. Photo-assisted self-chargeable aqueous Zn-ion energy storage device. *Chem. Eng. J.* **2024**, *500*, 156870.
[42] Roy, R.; R, G.; Basith, A.; Banerjee, R.; Singh, A. K. Self-rechargeable aqueous $Zn^{2+}/K^+$ electrochromic energy storage device via scalable spray-coating integrated with marangoni flow. *Energy Storage Mater.* **2024**, *71*, 103680.
[43] Roy, R.; Greeshma, R.; Dutta, P.; Mondal, I.; Banerjee, R.; Singh, A. K. Electrochromic and energy storage performance enhancement by introducing Jahn–Teller distortion: Experimental and theoretical study. *ACS Appl. Mater. Interfaces* **2024**, *16*, 39539–39550.
[44] Li, S. L.; Zhang, Z. X.; Wu, J. P.; Guo, X. L.; Chen, Y. Y.; Wang, C. H.; Yu, F.; Wang, Z.; Li, D.; Chen, Y. Stable Zn–$WO_3$ battery with a $ZnCl_2$ water-in-salt electrolyte. *J. Power Sources* **2023**, *560*, 232691.
[45] Li, Y. F.; Jiao, R.; Shen, X. Y.; Song, Y. H.; Ding, L.; Yang, G. D.; Shao, C. L.; Wu, X. L.; Zhang, J. P.; Deng, M. X. et al. Spherical metal mechanism toward revolution of Zn growth for ultrafast plating/stripping kinetics. *Energy Storage Mater.* **2023**, *62*, 102934.
[46] Li, J. H.; Qin, S. Q.; Xu, M.; Wang, W.; Zou, J. B.; Zhang, Y. G.; Dou, H. Z.; Chen, Z. W. Multifunctional dual-metal-salt derived ternary eutectic electrolyte for highly reversible zinc Ion battery. *Adv. Funct. Mater.* **2024**, *34*, 2402186.
[47] Yang, J. H.; Zhang, Y.; Li, Z. L.; Xu, X.; Su, X. Y.; Lai, J. W.; Liu, Y.; Ding, K.; Chen, L. Y.; Cai, Y. P. et al. Three birds with one stone: Tetramethylurea as electrolyte additive for highly reversible Zn‐metal anode. *Adv. Funct. Mater.* **2022**, *32*, 2209642.
[48] Huang, Q. J.; Wang, J. J.; Gong, H.; Zhang, Q. Q.; Wang, M. Y.; Wang, W. W.; Nshimiyimana, J. P.; Diao, X. G. A rechargeable electrochromic energy storage device enabling effective energy recovery. *J. Mater. Chem. A* **2021**, *9*, 6451–6459.
[49] Yang, X. H.; Zhang, C.; Chai, L. N.; Zhang, W. M.; Li, Z. Y. Bimetallic rechargeable Al/Zn hybrid aqueous batteries based on Al–Zn alloys with composite electrolytes. *Adv. Mater.* **2022**, *34*, 2206099.
[50] Lu, C.; Wang, Z. L.; Zhang, Y.; Tang, G.; Wang, Y.; Guo, X.; Li, J. J.; Wei, L. M. Aqueous aluminum-zinc hybrid ion batteries with urea-based hydrated eutectic electrolytes. *Nano Energy* **2024**, *120*, 109158.

This is an open access article under the terms of the Creative Commons Attribution 4.0 International License (CC BY 4.0, https://creativecommons.org/licenses/by/4.0/).

© The Author(s) 2025. Published by Tsinghua University Press.